High-speed atomic force microscopy reveals a three-state elevator mechanism in the citrate transporter CitS

Sourav Maity[a,1], Gianluca Trinco[b,1], Pedro Buzón[a], Zaid R. Anshari[b], Noriyuki Kodera[c], Kien Xuan Ngo[c], Toshio Ando[c], Dirk J. Slotboom[b,2], and Wouter H. Roos[a,2]

[a]Moleculaire Biofysica, Zernike Instituut, Rijksuniversiteit Groningen, Groningen 9747AG, The Netherlands; [b]Enzymology, Groningen Biomolecular Sciences and Biotechnology Institute (GBB), Rijksuniversiteit Groningen, Groningen 9747AG, The Netherlands; and [c]World Premier International Research Center Initiative Nano Life Science Institute (WPI-NanoLSI), Kanazawa University, Kakuma-machi, Kanazawa-shi 920-1192 Ishikawa, Japan

Edited by Simon Scheuring, Department of Physiology and Biophysics, Weill Cornell Medicine, New York, NY; received July 29, 2021; accepted December 21, 2021 by Editorial Board Member Nieng Yan

The secondary active transporter CitS shuttles citrate across the cytoplasmic membrane of gram-negative bacteria by coupling substrate translocation to the transport of two Na^+ ions. Static crystal structures suggest an elevator type of transport mechanism with two states: up and down. However, no dynamic measurements have been performed to substantiate this assumption. Here, we use high-speed atomic force microscopy for real-time visualization of the transport cycle at the level of single transporters. Unexpectedly, instead of a bimodal height distribution for the up and down states, the experiments reveal movements between three distinguishable states, with protrusions of ∼0.5 nm, ∼1.0 nm, and ∼1.6 nm above the membrane, respectively. Furthermore, the real-time measurements show that the individual protomers of the CitS dimer move up and down independently. A three-state elevator model of independently operating protomers resembles the mechanism proposed for the aspartate transporter Glt_{Ph}. Since CitS and Glt_{Ph} are structurally unrelated, we conclude that the three-state elevators have evolved independently.

membrane transporter | protein dynamics | high-speed atomic force microscopy | single-molecule biophysics

The cytoplasmic membrane forms a semipermeable barrier between the cellular interior and the periplasm of bacteria. The trafficking of molecules across the membrane is necessary for the cell's metabolism and is mediated by membrane transporters. These proteins are embedded in the lipid bilayer and undergo conformational changes leading to alternating exposure of the substrate-binding site to either side of the membrane. In secondary active transporters, the transitions between these conformational changes are strictly coupled to the binding and unbinding of not only the primary transported substrate but also a secondary substrate, which leads to their combined transport. Secondary substrates are usually protons or sodium ions of which membrane gradients are maintained in cells, which thereby provides the free energy gain necessary for substrate transport (1).

The secondary active transporter CitS mediates the accumulation of citrate in gram-negative bacteria by mechanistic coupling of substrate translocation to the transport of two Na^+ ions across the cytoplasmic membrane. In the pathogen *Klebsiella pneumoniae*, CitS is responsible for citrate uptake in the anaerobic citrate degradation pathway (2). CitS belongs to the 2-HydrocyCarboxylate Transporter family. Other members of this family are capable of transporting mono-, di-, and tricarboxylates containing a 2-hydroxy group. These proteins are involved in several energy conservation pathways such as citrate fermentation, malolactic fermentation, citrolactic fermentation, and oxidative malate decarboxylation (3–5). Crystal structures have been solved of CitS from *K. pneumoniae* and *Salmonella enterica* (6). The quaternary structure revealed that CitS is a homodimer, with each protomer consisting of two domains: a dimerization domain located centrally and a transport domain located peripherally (*SI Appendix*, Fig. S1). This dimeric structural arrangement of CitS leads to the presence of two identical transport routes per complex.

Before the first structure of CitS was revealed, the alternating access was explained as a "rocker switch" mechanism similarly to LacY and GlpT, two transporters for which crystal structures were available at the time (7, 8). The publication of the structure of CitS from *S. enterica* suggested that the translocation of the substrates occurs by an elevator mechanism, similarly to the aspartate transporters Glt_{Ph} and Glt_{Tk} (9, 10). The structure of CitS suggests that the dimerization domains serve as central membrane anchor, and the peripheral transport domains can move up and down through the bilayer during turnover as a rigid body. This movement leads to a displacement of the binding site by 17 Å perpendicular to the membrane plane, as well as a rotation by ∼35°, and shuttles the protein between the outward-facing and inward-facing conformations (11). This elevator-type mechanistic interpretation, however, was inferred solely from the static crystal structures,

Significance

As cellular membranes are impermeable to most molecules, transporter proteins are typically present in the membrane to transport small molecules in or out of the cell. Due to the small, nanometer size of these transporters, it is challenging to study their transport mechanism. Here, we use advanced microscopy approaches to study in real time and at the single-molecule level the mode of action of the dimeric CitS tranpsorter. Using high-speed atomic force microscopy, we visualize the dynamic, elevator-like movement of the transporter, and we reveal that the two protomers move independently. We also discovered an intermediate state, reminiscent of another, unrelated transporter, indicating that independent evolutionary pathways have led to similar three-state elevator mechanisms.

Author contributions: S.M., G.T., D.J.S., and W.H.R. designed research; S.M., G.T., Z.R.A., N.K., K.X.N., T.A., D.J.S., and W.H.R. performed research; S.M., G.T., and P.B. analyzed data; and S.M., G.T., D.J.S., and W.H.R. wrote the paper.

The authors declare no competing interest.

This article is a PNAS Direct Submission. S.S. is a guest editor invited by the Editorial Board.

[1]S.M. and G.T. contributed equally to this work.

[2]To whom correspondence may be addressed. Email: d.j.slotboom@rug.nl or w.h.roos@rug.nl.

This article contains supporting information online at http://www.pnas.org/lookup/suppl/doi:10.1073/pnas.2113927119/-/DCSupplemental.

Published January 31, 2022.

and dynamic experiments have not been reported to test this assumption. In this respect, high-speed atomic force microscopy (HS-AFM) (12–15) offers the advantage of probing membrane proteins in liquid in their lipidic environment with high spatial and temporal resolution (16, 17). Uptake experiments performed on CitS report an apparent turnover rate of roughly once every second at saturating conditions (*SI Appendix*, Table S1) (18). This rate is within the scanning capabilities of HS-AFM, and here, we report HS-AFM experiments directly visualizing the dynamics of citrate transport, at the single-molecule level, to unveil the molecular mechanism behind transport.

Results

Binding Order of Citrate and Sodium Ions to CitS. Although it is well established that citrate transport mediated by CitS is strictly coupled to the cotransport of two sodium ions (19), the order in which substrate and coupling ions bind is unknown. For a proper interpretation of our HS-AFM data, such information is essential. Therefore, we set out to deduce the binding order from measurements of the initial rates of uptake of radiolabeled citrate into proteoliposomes reconstituted with purified CitS. We determined the rates as a function of a wide range of citrate and Na^+ concentrations (Fig. 1*A* and *SI Appendix*, Table S1). These experiments provide a rich source of data on the kinetic mechanism, including the K_M values for citrate at different fixed Na^+ concentrations (K_M^{Cit}(app)). In Fig. 1*B*, a double logarithmic plot is presented of these apparent affinity constants as function of the concentration of Na^+. In such plots, linear relations are approached asymptotically in both the high– and low–Na^+ concentration extremes, with slopes of either zero or negative integers (20–22). The negative value of the slopes in the low- and high-concentration regime indicate the number of Na^+ ions that must bind before and after the citrate-binding event, respectively. For the discussion below (*Discussion*), the information on the number of sodium ions binding before citrate is most relevant. In Fig. 1*B*, the slope at low-Na^+ concentrations approaches −1, and therefore, we conclude that citrate-binding is preceded by an ordered step involving one Na^+ (20, 22).

Imaging the CitS Transporter by HS-AFM. To follow the conformational dynamics of CitS transporters by HS-AFM, we purified the dimeric protein and reconstituted it at high density in liposomes consisting of lipids extracted from *Escherichia coli*, the same lipid mixture in which CitS shows robust transport activity (Fig. 1). Upon adsorption onto a mica surface, the proteoliposomes formed a planar membrane bilayer with either the cytoplasmic side or the periplasmic side of the transporter facing up. The maximum protrusion of the transport domain when observed from the cytoplasmic side is expected to be <1.0 nm, while from the periplasmic side, this is >1.5 nm (23). Therefore, it is well distinguished, and we limited our observation to protein dynamics at the periplasmic side. Citrate transport by CitS is strictly coupled to the cotransport of Na^+ ions (11). In order to understand the role of both Na^+ and citrate in the transporting mechanism, we studied the membrane-embedded protein 1) in presence of saturated concentration of both Na^+ (300 mM) and citrate (150 μM) (*SI Appendix*, Table S1), 2) in presence of Na^+ but absence of citrate, and 3) in absence of both Na^+ and citrate. A typical surface topography image of CitS in presence of both Na^+ and citrate is depicted in Fig. 2*A*. Protrusions with a height of about 1.6 nm and an intradimer, peak-to-peak distance of about 6.8 nm were found. Comparison between the CitS features measured in presence of Na^+ and citrate with the crystal structure of the protein (23) revealed a similar height and spacing of the protrusions, indicating that they correspond to the transport domains (Fig. 2*B*). In contrast, when the protein was observed in absence of both Na^+ and citrate, the HS-AFM recording showed an increment in the intradimer spacing as can be seen in Fig. 2 *C*–*E*. Interestingly, while in presence of Na^+, almost no diffusivity of the dimers was observed, they became highly diffusive in the absence of Na^+ (Movie S1). Sodium-free conditions are nonphysiological, but this change in behavior indicates that Na^+ is playing a distinctive role in maintaining the stability of CitS in the membrane.

Role of Na^+ and Citrate in the Elevator Mechanism of CitS Transporting Domain. Next, we focused on the axial movement of the transport domains. Based on the crystal structures, it was proposed that these domains have two distinguishable conformational states: outward-facing (elevated) and inward-facing (down) (*SI Appendix*, Fig. S1) (24). To record the appearance and disappearance of the protrusions, which correspond to movements of the transport domains between the elevated and down states, we recorded HS-AFM movies at 2.5 frames per second in the presence of Na^+ and citrate. Snapshots of a recording are depicted in Fig. 3*A* and indeed reveal alternation between outward- and inward-facing states. Kymograph representations of eight distinguishable individual domains from

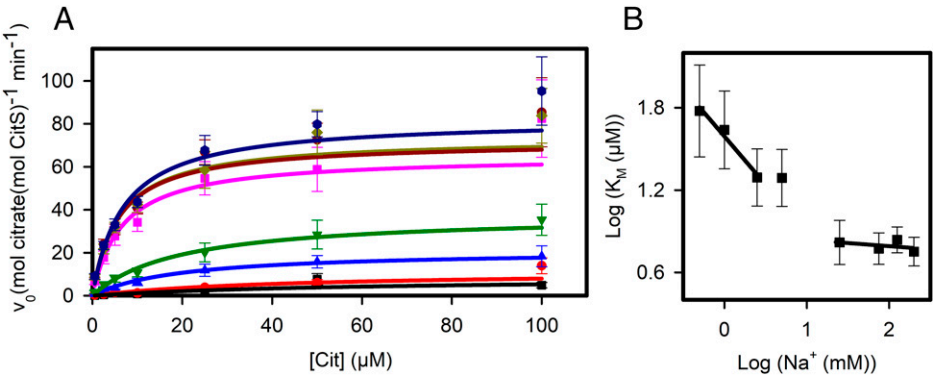

Fig. 1. Kinetic studies of CitS. (*A*) Citrate transport rates reported in *SI Appendix*, Table S1 plotted as a function of citrate concentration. The lines represent the fits of the Michaelis–Menten equation to the data for uptake at Na^+ concentrations of 0.5 mM (black), 1 mM (red), 2.5 mM (blue), 5 mM (cyan), 25 mM (magenta), 75 mM (yellow), 125 mM (dark blue), and 200 mM (brown). (*B*) Dependence of the apparent affinities (K_M) for citrate obtained from the fitted curves in *A*, plotted against the Na^+ concentration in which they were obtained in a double logarithmic scale. The lines represent linear fits at low- and high-[Na^+] regimes. The values obtained from the linear regression are −0.73 and −0.04 for the low- and high-[Na^+] regime, respectively. The values will tend to an integer number at infinitely low and high [Na^+]; therefore, we approximated such value to the closest integer number. The data points are the average of triplicate measurements, and the error bars represent the SEM.

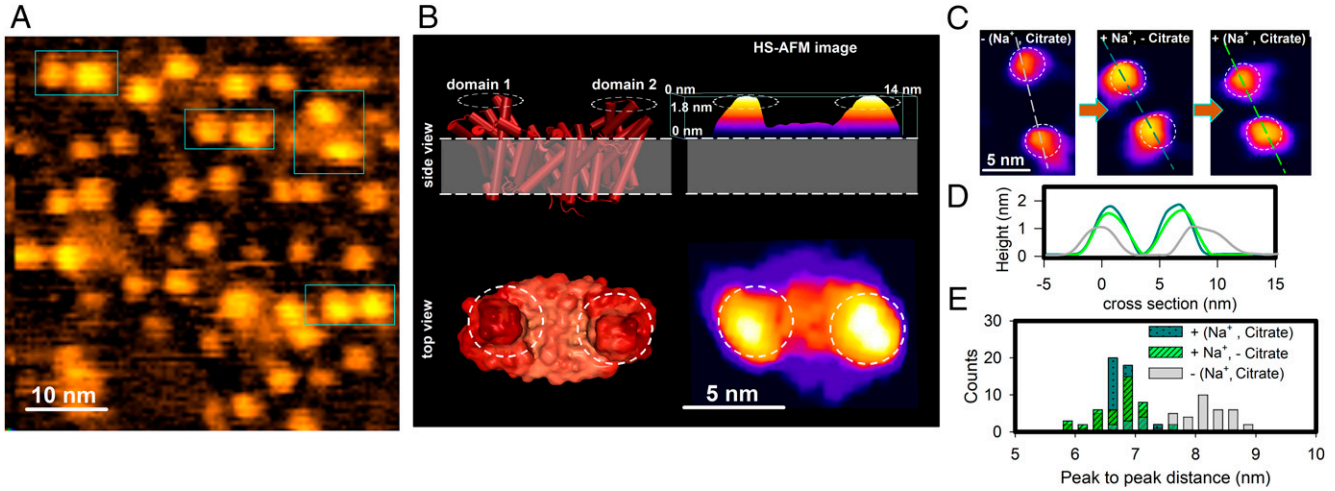

Fig. 2. Membrane protrusion of CitS transporters imaged by HS-AFM. (*A*) HS-AFM image of the CitS transporter dimers (yellow/brown) protruding out of the membrane (black). Several dimers are highlighted by rectangular boxes. The image was taken in presence of Na^+ and citrate. (*B*) Comparison of the reported CitS surface protrusion as obtained by X-ray diffraction (PDB [Protein Data Bank]: 5X9R) (23) with the AFM data—in presence of Na^+ and citrate—shows a good fit between the two approaches. (*C*) Different intradimer distances (peak-to-peak distances between transporting domains) are observed for different conditions. (*D*) Cross-sectional height profile of images in *C*. (*E*) Distribution of peak-to-peak distances between the transporting domains of more than 40 individual dimers for each condition.

four dimers (Fig. 3 *B* and *C*) show the transitions between the states over time.

For a more-quantitative analysis of the protruded height of the transport domains, we measured the height of the protrusion above the membrane frame by frame (*SI Appendix*, Figs. S2 and S3 and *Methods*). Fig. 4 *A*–*C* shows example traces of these measurements along with histograms of the height measurements of all analyzed CitS molecules. In the absence of Na^+ and citrate (nonphysiological condition), the transporter exhibits a height of 1.0 ± 0.2 nm and does not show significant movement in the axial direction (Fig. 4*A*). Na^+ alone is sufficient to trigger the elevator movement of the transport domain in CitS (Fig. 4*B*). Unexpectedly, instead of showing a bimodal height distribution (for up and down states) as deduced from the crystal structures (11, 23, 24), three distinguishable distributions at ∼0.5 nm, ∼1.0 nm, and ∼1.6 nm were observed in the presence of Na^+ (Fig. 4*C*). After the addition of citrate, similar peaks as for the Na^+-alone situation were observed, but the distribution over the peaks was different. In order to characterize the data further, each data point was assigned to one of the three observed states: elevated, intermediate, or down (Fig. 4 *A*–*C*, *Left*). Fig. 4*D* and Movie S3 show AFM data of these three distinct states. The probability of finding the domains in one of these states is shown in Fig. 4*E*. The elevated state has the highest probability in both Na^+-containing conditions; however, the probability of finding the domain in the intermediate state is relatively higher when citrate is present. Interestingly, the domain has similar probability to be found in the down state both in absence and presence of citrate. This observation suggests that even when the absence of citrate does not allow the transporter to go through the entire alternating-access transport cycle, Na^+ alone is sufficient to promote the conformational switch in the elevator mechanism.

Next, we looked into the potential cooperativity in movement of the two protomers of the CitS dimer (*SI Appendix*, Fig. S4). Comparing the idealized traces of individual protomers suggests that the protomers act independently (*SI Appendix*, Figs. S4 and S5*A* and Fig. 4 *B* and *C*). However, it is often observed that one of the protomers is more active than the other within the period of recording (*SI Appendix*, Fig. S4). We estimated that a fast-protomer shows four times more jumps to the down state than the slower protomer (*SI Appendix*, Fig. S4*B*). Quantifying the relative frequencies of all six conformation combinations of all measured dimers (*SI Appendix*, Fig. S5*B*) and the position of one protomer with respect to the other (*SI Appendix*, Fig. S5*C*), no clear signs of cooperativity are observed. It can be concluded that the protomers move up and down independently of each other. Therefore, we can analyze their dynamics separately. To scrutinize these protomer dynamics further, the relative transition frequencies from one state to another were determined (Fig. 4*F*). While the transporter shows elevator movements in both the presence and absence of citrate (with Na^+ present in both cases), the six possible state transitions revealed major differences in the two conditions. In particular, in absence of citrate, the most-frequent transition is between the elevated and down states. In contrast, in presence of citrate transitions between elevated and intermediate states are the most-frequently occurring ones. The transition between intermediate and down states exhibits relatively low frequencies for both conditions. Our observations reveal that while Na^+ is playing a pivotal role in switching the transporting domain from the elevated to down state and vice versa, the presence of citrate makes this domain to fluctuate more in between elevated and intermediate states.

Dynamics of Transporting Domain in CitS Transporter. In order to validate our interpretation of the existence of three distinguishable states we used an infinite Hidden Markov Model (25) (iHMM; *Methods*), which allows analyzing the experimental time traces without any constraints in the number of states. A small majority of the HS-AFM height-time traces analyzed by the iHMM successfully yielded three states (*SI Appendix*, Fig. S6*A*), but for certain traces, the least-populated state could not be recognized by the iHMM (*SI Appendix*, Fig. S6*B*). These concerned the down state in presence of Na^+ and citrate and the intermediate state in presence of Na^+ alone. The analysis of such traces, showing a very limited number of visits to the third state, yielded two-state trajectories instead (*SI Appendix*, Fig. S6*B*). A comparison of tracking three states using iHMM and idealized traces has been depicted in *SI Appendix*, Fig. S7 for both Na^+-alone as well as Na^+ and citrate conditions. Next, we have determined the dwell-time distribution for individual states in presence and

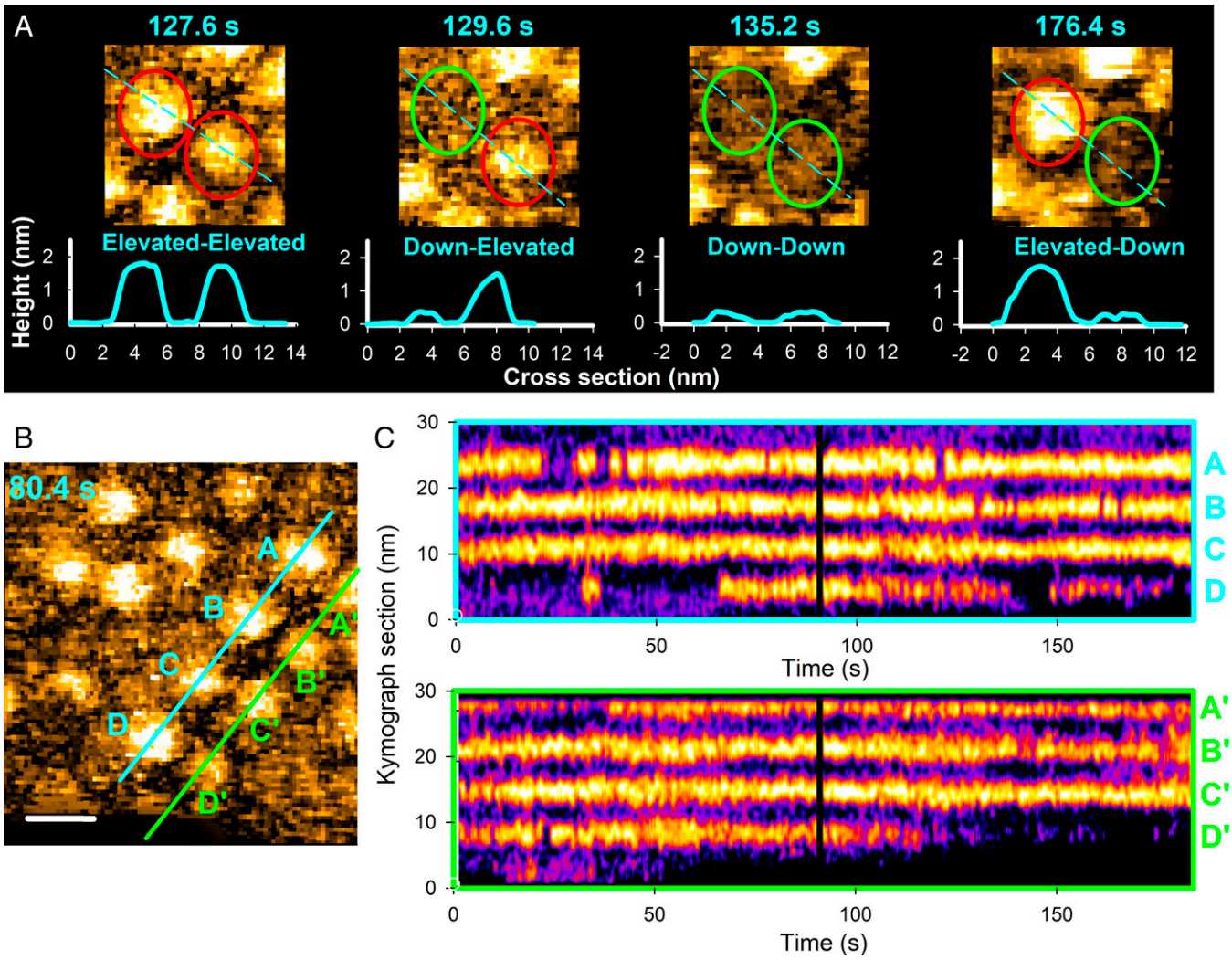

Fig. 3. Direct visualization of CitS transporting domain elevator motion. (*A*) Snapshots of a single dimer from Movie S2 revealing the dynamics of the transporter domains. Red and green circles are indicating the elevated and down states, respectively. (*B*) Example of a frame from Movie S2 with four dimers next to each other and an indication of the cross-sectional profile from which the kymograph in *C* is obtained. (Scale bar, 5 nm.) (*C*) Two parallel kymographs of the height of transporting domains of four different dimers (A and A′, B and B′, etc.). The black vertical line in the panels around 90 s are due to two missing frames resulting from a loss of contact between AFM tip and surface. Imaging speed is 2.5 fps.

absence of citrate (both containing Na^+; *SI Appendix*, Fig. S8) by using idealized traces. The dwell-time distributions were well represented by a single exponential function, as expected for a Markovian system, and yielded the stochastic rate constants for leaving a specific state. This rate appears to be similar in absence and presence of citrate except for the intermediate states. To relate the dynamics of the transport domain with its function, we determined the rate constants for transitions between states by calculating the transition probability matrix of the idealized traces (*Methods*). Rate constants were also obtained from the iHMM analysis, and the comparisons are depicted in *SI Appendix*, Table S2 (in presence of Na^+ only) and *SI Appendix*, Table S3 (in presence of Na^+ and citrate). A similar trend for both approaches is found. Using this data, we evaluated the free energy differences between the corresponding states (*Methods* and *SI Appendix*, Fig. S9). In absence of citrate, there is 1.6 k_BT of free energy difference for a transition from the elevated to down state ($\Delta G^0_{ele\text{-}down}$); 2.5 k_BT of free energy difference for a transition from the elevated to intermediate state ($\Delta G^0_{ele\text{-}inter}$); and −0.3 k_BT of free energy difference for a transition from the intermediate to down state ($\Delta G^0_{interdown}$). When citrate is present, the estimated free energy differences are 1.4 k_BT, −0.2 k_BT, and 1.3 k_BT, respectively (*SI Appendix*, Fig. S9). This reveals that independent of the presence or absence of citrate, a similar value of free energy difference between elevated and down state is observed, while for transitions involving the intermediate state, significant differences arise.

Discussion

Using HS-AFM, we studied the functional mechanism of CitS transporters, and our real-time imaging approach revealed that the proposed elevator mechanism (6, 11, 23) is real. Surprisingly, while the crystal structures suggested a two-state elevator mechanism, it turns out that the dynamic CitS elevator mechanism goes through three discrete states, termed here elevated, intermediate, and down. The three states are distinguished solely by the observed elevation of the transport domains in the AFM measurements and do not directly relate to their functional states (apo, bound, nonoccluded, occluded, etc.). Indeed, multiple functional states could be associated with the same elevation.

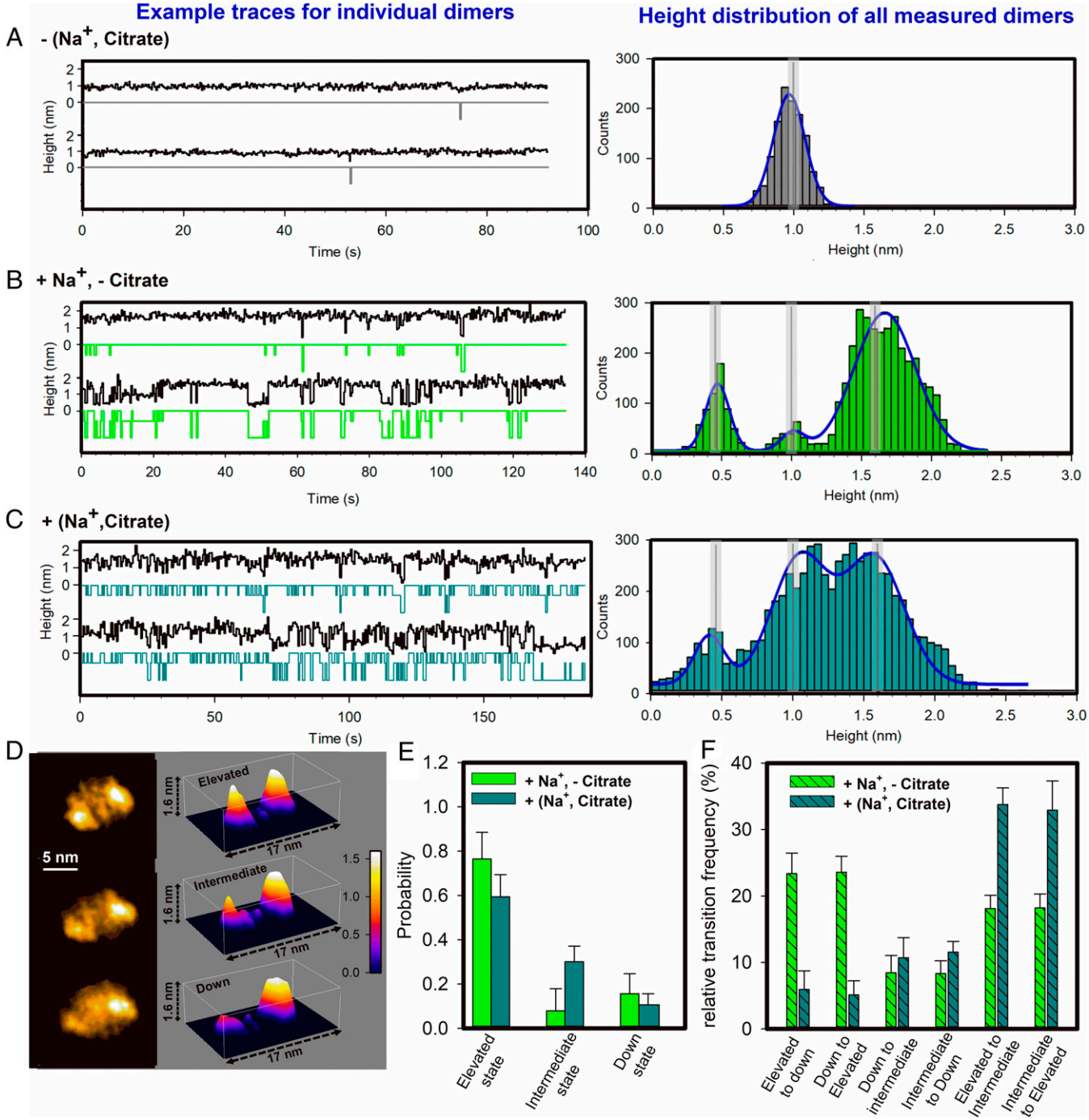

Fig. 4. States of transporting domains captured under the HS-AFM in real time. (*A*–*C*) (*Left*) Real height evolution over time and idealized traces for a single dimer. For each condition, two examples are provided. (*Right*) Histograms of the real height distributions for all measured dimers. Peaks are located at 1.0 ± 0.2 nm without Na^+, at 0.5 ± 0.1 nm, 1.0 ± 0.1 nm, and 1.7 ± 0.3 nm in the presence of Na^+, and at 0.4 ± 0.2 nm, 1.1 ± 0.3 nm, and 1.6 ± 0.3 nm in the presence of both Na^+ and citrate. (*D*, *Top*) HS-AFM images and corresponding three dimensional (3D)-rendered surface topography depicting three different elevation states of one of the transporting domains (*Left*) of a CitS dimer in the presence of Na^+ and citrate. The *Right* domain is elevated all the time in this example. (*E*) Comparison of probability of finding the transporting domain in one of the three states. (*F*) The frequency of transition between two states in absence (light green) and presence (dark cyan) of citrate. Idealized traces are used to derive the frequencies in *E* and *F*.

Unexpectedly, this three-state elevator mechanism resembles what has been found for the aspartate transporters Glt_{Ph} and Glt_{Tk}, in which crystal or cryogenic electron microscopy (cryo-EM) structures have resolved the three positions of the elevator (10, 26, 27). In the case of Glt_{Ph}, HS-AFM studies showed that the three states were indeed visited under near-physiological conditions (28). Also, the approximate seconds time scale of the movements up and down in CitS and the lack of cooperativity in the elevator-like movements of the individual protomers in the homodimeric CitS assembly resemble the functional properties of the homotrimeric aspartate transporter Glt_{Ph} and Glt_{Tk} (10, 16, 29). These similarities are surprising, because the aspartate transporters are not related in sequence and structural fold to CitS. Therefore, the use of three-state elevator

mechanisms, lack of cooperativity, and seconds time scale of the movements appear to have evolved in parallel. The observation that two structurally unrelated proteins operate using a three-state mechanism may suggest that there is a constraint that precludes a two-state mechanism. One speculative possibility is that it is more difficult to prevent ion leaks in a two-state mechanism, but more work is needed to substantiate such speculation. A number of other transporters also use elevator-type mechanisms, and it is worth testing in future whether they also visit more structural states than currently elucidated at high resolution (30–32). Finally, increased temporal resolution using line-scan HS-AFM could improve the kinetic analysis (28), including a better view on the energy landscape of the different states.

The elevator movements of CitS were observed in the presence of Na^+ and in the presence of both Na^+ and citrate, while in absence of both ligands, the dimeric protein adopts a conformation in which the transport domains of both protomers are immobile and are separated further than in the conditions that show dynamic behavior. Complete absence of Na^+ is nonphysiological, and therefore, we do not take the observed immobility into account for the proposed mechanism of transport (see below). We speculate that the structural integrity of CitS is compromised in the absence of Na^+, resulting not only in wider separation of the protomers but also in increased diffusion through the membrane.

In the conditions in which dynamic elevator movements are observed, the elevated position at 1.7 nm is dominant in presence of Na^+, while in the presence of Na^+ and citrate, the intermediate position at about 1 nm exhibits similar likelihood as the elevated state. Fig. 5 shows the energy landscape of the transporter in absence and presence of citrate, visualizing the free energy differences between the three states. Next to the citrate-dependent difference in rates from and to the intermediate state, it can also be seen that the presence of citrate slightly flattens the energy landscape, easing transitions. In the presence of citrate and Na^+, the transporter visits the three elevator states. It is likely that the carrier in the elevated state is fully loaded, because of the saturating concentrations of substrate and coion. A fully loaded elevated state is also consistent with the observations from the crystal structure in which both Na^+ and citrate are bound to the outward-facing transport domain (11). In physiological conditions, it is expected that the binding of ligands from the environment occurs in this state (11, 23). The down state likely corresponds to the inward state observed in the crystal structure. In physiological conditions, citrate and Na^+ are released into the cytoplasm from this state. However, because, in both HS-AFM and crystallization condition, the concentrations of substrate and coion were saturating and no membrane gradient was present, the down state must represent the inward-loaded state as observed in the crystal structures (11, 23). Movements between the up and down states in the presence of citrate and Na^+ occur directly or via the intermediate state. The possibility to bypass the intermediate state when moving between the down and elevated states resembles what was observed for the aspartate transporter Glt_{Ph} (16). It is not clear whether binding and unbinding of transported cargo can also take place in the intermediate state or that the state takes an occluded conformation. Further structural characterization is needed to answer this question.

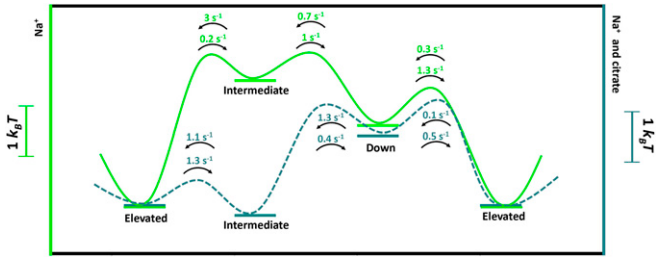

Fig. 5. The energetics and dynamics of CitS transporter. Comparison of the free energy landscape of CitS transporter in absence (light green) or presence (dark cyan) of citrate. The baseline of the landscape is relative and was calculated using a kinetic analysis of the idealized traces. Refer to *SI Appendix*, Tables S2 and S3 for calculations of the kinetics using iHMM method.

In the presence of Na^+ but in the absence of citrate, CitS can bind at least one sodium ion (Fig. 1), as determined in the kinetic analysis. With only Na^+ bound, cycling between inward- and outward-exposed conformations would lead to uncoupled leakage of Na^+, and therefore, these transitions should not occur. Surprisingly, the HS-AFM data revealed that movements between elevated and down states take place in the presence of only Na^+. There are two possible explanations for this observation. The first is that full movement between elevated and down states can take place with sodium ion(s) bound but that the sodium ion(s) cannot be released once the opposite side is reached. Although theoretically possible, this explanation is not consistent with the known crystal structures that revealed exposed binding sites in the outward and inward states (11, 23). The alternative explanation is that the sodium ion concentration is not fully saturating in the absence of citrate. This is a well-known phenomenon in other sodium-coupled transporters such as Glt_{Ph} (10), in which sodium ions bind weakly and cooperative binding of aspartate increases the apparent affinity for Na^+. It is noteworthy that the equilibrium binding constant of Na^+ in the absence of citrate (defined by the K_D) is difficult to determine but likely is of much-lower affinity than the apparent K_M values for Na^+ observed under transport (nonequilibrium) conditions (11, 22, 33). Thus, in the presence of only Na^+, a fraction of the transporters is likely unoccupied and adopts an apo conformation, which has not been resolved in the available crystal structures. This conformational movement between outward and inward states is possible, as reorientation of the empty carrier is part of the transport cycle of sodium-coupled symporters. The HS-AFM data show that the intermediate state may be visited on the way, although it is less favored than when citrate is also bound. In the sodium-bound conformation, the transporters would not be able to move between elevated and down states, but it is possible that they can still move between outward and intermediate or inward and intermediate states without being able to complete the full elevator movement. The inability to fully move when only Na^+ is bound can be explained from the crystal structures. In the Na^+-only state, two arginine residues in the binding-side region (R402 and R428) likely prevent the elevator movement by exposing the sidechains at the interface between the scaffold and transport domains. In the fully loaded state (citrate plus Na^+-bound), these arginine side chains are more buried, because they interact directly with carboxylate groups of the substrate. In the apo state, the side chains may also be buried as they can now occupy the empty Na^+-binding sites. In both cases, the elevator movement would not be blocked.

By studying the dynamics of the CitS transporter, we were not only able to reveal the independent movement of the individual protomers but also that the elevator movement displays three different states. These unexpected insights raise the question of how other transmembrane transporters function, and the reported HS-AFM approach paves the way to address this question.

Methods

Expression and Purification of CitS. The expression vector pBAD_CitS (4) was transformed in *E. coli* MC1061 competent cells, and the recombinant strain was then cultivated in Luria-Bertani broth (LB) medium supplemented with 100 μg/mL ampicillin. The protein expression was induced with 0.05%

L-arabinose when the culture reached an optical density of 0.8 at 600 nm. Three hours after induction, cells were harvested (6,500 RPM, 4 °C, 15 min, Beckman JLA 9.1000 rotor) and resuspended in 20 mM Tris·HCl (pH 8), then cells were either frozen in liquid nitrogen or directly broken. The harvested cells were supplemented with 10 μg/mL of DNase, 200 μM phenylmethylsulfonyl fluoride (PMSF), and 1 mM $MgSO_4$ before being passed through a Constant System cell disruptor precooled at 4 °C and operated at 20 KPSI (Constant Systems Ltd., Daventry, United Kingdom). The remaining unbroken cells and cell debris were separated by centrifugation (7,500 RPM, 4 °C, 20 min, Beckman JLA 25.50 rotor), and the crude cytoplasmic membranes in the supernatant were then pelleted (40,000 RPM, 4 °C, 150 min, Beckman 45 Ti) and finally resuspended in 20 mM Tris·HCl (pH 8) for storing at −80 °C. The crude membranes containing CitS were solubilized in solubilization buffer (50 mM Tris·HCl [pH 8], 300 mM KCl, 15 mM imidazole [pH 8], and 1% n-dodecyl-β-D-maltoside (DDM)) on a rocking platform at 4 °C for 45 min, and the solution was then centrifuged (55,000 RPM, 4 °C, 30 min, Beckman MLA 55 rotor), and the supernatant was incubated for 1 h with 500 μl of pre-equilibrated (50 mM Tris·HCl [pH 8], 300 mM KCl) Ni-Sepharose resin. The mixture was then loaded on a Poly-Prep column (Bio-Rad), the unbound protein solution was let flow through, and the nonspecifically bound proteins were washed with 20 CV of cold washing buffer (50 mM Tris·HCl [pH 8], 300 mM KCl, 60 mM imidazole [pH 8], and 0.15% DDM). The protein was eluted using consecutive addition of 300, 750, and 400 μl of cold elution buffer (50 mM Tris·HCl [pH 8], 300 mM KCl, 500 mM imidazole [pH 8], and 0.15% DDM), the second fraction was then further purified by size-exclusion chromatography (SEC) on a Superdex 200 increase 10/300 GL (GE Healthcare) column using SEC buffer (10 mM Hepes-KOH [pH 8], 100 mM KCl, and 0.15% DDM) as running buffer, and the temperature was kept at 4 °C for the whole process. Uptake assays were performed to assess that CitS retained its activity after purification.

The purified protein was added to Triton X-100 (10%) (34) destabilized liposomes (*E. coli* polar extract supplemented with egg phosphatidylcholine in a ratio of 3:1 [*E.coli*:PC] in a protein/lipid ratio of 1:800). The protein and lipid mixture were incubated at room temperature for 30 min, then the detergent was removed by addition of BioBeads in three steps: 15 mg/mL of BioBeads was added and the solution was incubated for 30 min at 4 °C, then 19 mg/mL BioBeads was added followed by O/N incubation at 4 °C. Finally, 29 mg/mL BioBeads was added followed by 120 min incubation at 4 °C. BioBeads were then removed, and the proteoliposomes were pelleted (80,000 RPM, 25 min, 4 °C, Beckman MLA80) and resuspended in 10 mM potassium phosphate buffer (pH 7) to a final lipid concentration of 20 mg/mL. The proteoliposomes were subjected to three cycles of freeze-thawing using liquid nitrogen and extruded 11 times through a 400-nm pore size polycarbonate filter and pelleted again (80,000 RPM, 25 min, 4 °C, Beckman MLA80). The liposomes were resuspended to a concentration of 100 mg/mL, and 10 μL finally was added to 1 mL of solution containing 10 μM citrate (of which 0.5 μM was labeled with ^{14}C), 200 mM NaCl, and 10 mM potassium phosphate buffer (pH 7). The reaction was stopped by quickly adding 200 μL of reaction in 2 mL of ice-cold quenching buffer containing 10 mM potassium phosphate buffer (pH 7) and 200 mM KCl after 10, 20, 30, 60, and 90 s from the start of the reaction. The quenched reaction was filtered through a BA 45 nitrocellulose filter and then washed with 2 mL of quenching buffer. The filters were finally dissolved in scintillation mixture Ultima Gold (Perkin-Elmer), and the β-decay from the radiolabeled substrate was counted.

CitS Reconstitution in Liposomes for Kinetic Analysis. The lipids used to reconstitute CitS contained a 3:1 mixture of *E.coli*:PC (Avanti). Liposomes were homogenized by extruding 11 times through a 400-nm pore size filter and subsequently diluted to 5 mg/mL in 50 mM potassium phosphate buffer, pH 7. To allow the insertion of the protein into the bilayer, the lipids were destabilized by step-wise addition of 10% Triton X-100, while scattering was followed at a wavelength of 540 nm. The titration was stopped once the absorption signal decreased to about 60% the maximum value reached. Purified protein was added at a protein:lipid ratio (wt/wt) of 1:800. The protein lipid mixture was incubated for 30 min at room temperature, and then the detergent was removed by addition of BioBeads in three steps: First, 15 mg/mL BioBeads was added followed by incubation for 60 min at 4 °C, then 19 mg/mL BioBeads was added followed by overnight incubation at 4 °C. Finally, 29 mg/mL BioBeads was added followed by 120 min incubation at 4 °C. BioBeads were then removed, and the proteoliposomes were pelleted (80,000 RPM, 25 min, 4 °C, Beckman MLA80) and resuspended in 50 mM potassium phosphate buffer (pH 7) to a final lipid concentration of 20 mg/mL. The proteoliposomes were subjected to three cycles of freeze-thawing using liquid nitrogen and stored in liquid nitrogen until use.

CitS Steady-State Rates Measurement. The luminal buffer in each proteoliposome preparation was changed to 10 mM potassium phosphate buffer (pH 7) and 200 mM KCl. The proteoliposomes were first pelleted (80,000 RPM, 25 min, 4 °C, MLA80) and then resuspended in the desired luminal buffer. Three freeze-thaw cycles were performed in order to allow the exchange of buffer in the luminal area of the proteoliposomes. The solution was then extruded 11 times through a filter with 400-nm pore size in order to obtain homogeneously sized unilamellar vesicles, which were pelleted (80,000 RPM, 25 min, 4 °C, TLA100.3) and resuspended to a final lipid concentration of 100 mg/mL. Steady-state rates were measured at different concentrations of substrate and coions. An array of conditions was prepared as shown in *SI Appendix*, Table S1. The blank measurement for each condition was measured by pipetting the liposome on the side of a test tube containing 200 μL of reaction buffer and subsequently flushing them in the reaction buffer with 2 mL of ice-cold quenching buffer (10 mM potassium phosphate buffer [pH 7] and 200 mM KCl). The content of the tube was then poured onto a BA 45 nitrocellulose filter which was then washed with 2 mL of quenching buffer. The filters finally dissolved in scintillation mixture Ultima Gold (Perkin-Elmer), and the β-decay from the radiolabeled substrate was counted.

The value for each uptake rate reported in *SI Appendix*, Table S1 represents the average and SE of three independent biological replicates, each constituted by two or three technical replicates. The substrate-dependent uptake rates obtained at fixed concentration of Na^+ were plotted as a function of citrate and fitted to the Michaelis–Menten equation to obtain apparent K_M (K_M^{Cit} (app)) values for different [Na^+]. The statistical analysis of the data was executed in Origin8.

High-Density Reconstitution of CitS on Membrane. To achieve a densely packed membrane patch, we followed the procedure by Kebbel and colleagues (24). This procedure yielded densely packed liposomes, which didn't diffract the electron beam when analyzed with negative-staining electron microscopy. The detergent-solubilized CitS (concentrated to 1.4 mg/mL) and *E. coli* polar extract lipid previously solubilized (10 mg/mL solubilized in 2% DDM) were mixed at protein to lipid ratios of 1:2, 1:1, and 2:1. The mixture was incubated on ice for 12 h and then loaded into glass tubes sealed on one end with parafilm and the other end with a 14-kDa molecular weight cut-off (MWCO) membrane. The sample was dialyzed against 20 mM NaAcetate, pH 4.5, 500 mM NaCl, 15 mM $MgCl_2$, 2 mM DTT, and 2 mM NaN_3, and the dialysis buffer was refreshed every 24 h. The dialysis was carried out at different temperatures over 4 d of dialysis (24 h at 10 °C, 48 h at 34 °C, and 24 h at 10 °C). The AFM experiments were executed at pH 7, as this is expected to yield optimal transporter activity (11). To confirm that the low pH used for the reconstitution does not irreversibly inactivate CitS, we incubated proteoliposomes (prepared as stated above for the kinetic analysis) (*CitS Reconstitution in Liposomes for Kinetic Analysis*) for 1 h at pH 4.5 or at pH 7. Subsequently, transport of citrate was measured for both preparations at pH 7, which indicated that transport activity is largely restored for liposomes prepared at pH 4.5 (*SI Appendix*, Fig. S10).

AFM Experiments. The AFM images were acquired in amplitude modulation tapping mode in liquid, using high-speed atomic force microscopes (both a home-built system of T.A. and a commercial system from Research Institute of Biomolecule Metrology, Japan) (35, 36). The HS-AFM imaging was performed using small silicon nitride cantilevers (BL-AC10-DS, Olympus, Japan) with a nominal spring constant of ∼0.1 N/m^{-1} and a resonance frequency of ∼400 to 500 kHz in buffer. The probe tip was grown on top of the cantilever by electron beam deposition (37) using an electron beam lithography system (ELS-7500UK, Elionix, Japan). The tips were then sharpened using plasma cleaning for 30 s. The applied-imaging forces were controlled by using a cantilever setpoint amplitude of 0.8 nm with 1-nm free oscillation amplitude. During incubation and imaging, a buffer containing 50 mM potassium phosphate, pH 7, was used, supplemented with 300 mM NaCl or 300 mM NaCl and 150 μM citrate, pH 7, when indicated. Prior to HS-AFM recording, the CitS-reconstituted liposomes were incubated on a freshly cleaved mica for 15 to 20 mins. After incubation, the surface was cleaned thoroughly using the pH 7 phosphate buffer (when appropriately supplemented with Na^+ or Na^+ and citrate). The buffer conditions were changed (adding Na^+ or adding Na^+ and citrate) by using a syringe pump connected to a 55-μl measurement chamber. Buffer flow was kept constant at 60 μl/min, and a pumping time of about 5 min to assure a complete buffer exchange. Measurements were started after buffer exchange had finished.

AFM Data Analysis. The acquired AFM images were analyzed using home-built software of Kanazawa University (Kodec), Igor Pro, and ImageJ with additional home-written plug-ins. Height measurements were performed on

raw images after tilt correction. The evaluation of real heights of a single transporting domain was performed frame by frame by calculating the height of the domain and subtracting the height of the membrane in close vicinity (*SI Appendix*, Fig. S3 *A* and *B*). The height of a single transporting domain was calculated by tracking individual protomers and measuring the maximum height in the region of interest (15, 38). To exclude the possibility of surface fluctuations interfering with the height measurements, we estimated the distribution of roughness of the membrane surface over time. This resulted in a single Gaussian distribution around 0.02 ± 0.3 nm (*SI Appendix*, Fig. S3*C*). Given an SD of 0.3 nm, the multipeak fits in Fig. 4 *A*–*C* reveal clearly distinguished peaks. For the data in the right panels of Fig. 4 *A*–*C*, the height dynamics of, respectively, 5, 8, and 14 dimers were analyzed for over 3,000 s for each condition. All stated errors in the text are SDs unless otherwise mentioned. The HS-AFM height versus time traces were idealized in Fig. 4 *A*–*C*, *Left* by using threshold conditions for individual peaks measured from the overall height distribution in Fig. 4 *A*–*C*, *Right*. The conditions for idealization were used as follows: height < 0.6 nm for down state, 0.6 < height > 1.35 nm for intermediate state, and height > 1.35 for elevated state. Occasionally, the movement of the transporting domain seems to be influenced by neighboring protomers. However, no significant difference in the dynamics was observed when analyzing the proteins in a high-population region compared to those observed at low density. The presented HS-AFM movies were drift corrected using "template matching," a built-in plugin in ImageJ.

Kinetic Analysis of Idealized Traces. The idealized traces of individual protomers obtained by thresholding were used to obtain the transition probability matrix and dwell-time distributions (*SI Appendix*, Fig. S6), as described in ref. 39. A custom-written MATLAB script was used to compute the counting matrix (M) from the individual-state trajectories, in which every matrix element (M_{ij}) represents the number of transitions from state *i* to state *j* after a certain time *t* (frame rate). The *M* matrix was row normalized to obtain the transition probability matrix, with its individual terms (P_{ij}) giving the frequency of the protomer transition from state *i* to state *j*. The expression $k_{ij} = -\ln(1 - P_{ij})/t$ was used to estimate the rate constants (k_{ij}) governing the individual-state transitions (*SI Appendix*, Tables S1 and S2).

Hidden Markov Analysis. The iHMM (25) was applied to analyze the HS-AFM height versus time traces of individual protomers. This generalization of the HMM, based on Bayesian nonparametrics, allows analyzing the experimental time traces without a priori setting of a specific number of states. All traces were analyzed by the iHMM for an initial number of states = 10, which were reduced by the algorithm to two or three states before the first 500 iterations. We note that for particularly short traces in which a certain state was only detectable by few transient visits, the iHMM was unable to assign the third state (*SI Appendix*, Fig. S6*B*). After these burn-in periods of 500 iterations, additional 1,500 to 2,000 iterations were performed to compute the transition probability matrix for every trace. Transition-concentration (α) and base-concentration (γ) parameters were varied between 1 and 10^3 and 10^{-1} and 10^{-4}, respectively, keeping the rest of the parameters as default (25). The rate constants derived from the iHMM analysis are presented in *SI Appendix*, Tables S2 and S3. It is important to note that given the temporal resolution (300 to 400 ms per frame), the characterization of short-lived states will give rise to some uncertainties, and very short-lived states will not properly by identified by our approach. Unless otherwise mentioned, all presented errors are in terms of SD.

Estimation of Free Energy Difference. The estimation of free energy difference ΔG^0 between state *i* and *j* is calculated as:

$$\Delta G^0{}_{i-j} = -ln(k_{i-j}/k_{j-i}) * k_B T,$$

where k_{i-j} is the estimated rate constant for the transition from *i* to *j* and k_{j-i} is the estimated rate constant for the transition from *j* to *i*. k_B is the Boltzmann constant and *T* absolute temperature.

Discussion of the Kinetic Analysis Using Idealized and/or iHMM. We have used both the idealized traces and iHMM to describe the three-states mechanism of citrate transporter CitS. While iHMM allowed us to identify three states without defining a prerequisite number of states as input parameter, the method fails to identify three states for some short traces, in which transition to one of the states is present but not for a significant amount of time. Examples are shown in *SI Appendix*, Fig. S6. It is observable that the trace *SI Appendix*, Fig. S6*A* shows a reasonable transition between the states (also observable in the histogram); as a result, iHMM could successfully detect three states. However, the trace in *SI Appendix*, Fig. S6*B* B has only few visits to the down state (also observable in the histogram) within the duration of recording, causing iHMM not being able to detect three states. In order to include all possible transitions and to calculate the transition frequencies, we have used idealized traces. Comparative trajectories by fitting iHMM and idealized traces are shown in *SI Appendix*, Fig. S7. The kinetic analysis was done using both idealized traces and using iHMM method and are summarized in *SI Appendix*, Tables S2 and S3.

Data Availability. All study data are included in the article and/or supporting information.

ACKNOWLEDGMENTS. We acknowledge support through an Dutch Research Council (NWO) Vidi grant to W.H.R. and TOP grant to D.J.S., and an Marie Skłodowska-Curie Actions (MSCA) Individual fellowship (INTERACT 751404) to S.M. S.M. acknowledges 7th Bio-AFM summer school organized by Nano Life Science Institute (NanoLSI), Kanazawa University, Japan, and a Visiting Scientist position at NanoLSI, supported by a grant from the MEXT Japan (15K21711 to T.A.). Z.A.H. and D.J.S. acknowledge support form European Union's Horizon 2020 research and innovation programme under the Marie Skłodowska-Curie Actions grant agreement no. 860954 (Neurotrans).

1. B. Poolman, W. N. Konigs, Secondary solute transport in bacteria. *Biochim. Biophys. Acta.* **1183**, 5–39 (1993).
2. P. Dimroth, A. Thomer, Citrate transport in *Klebsiella pneumoniae*. *Biol. Chem. Hoppe Seyler* **367**, 813–823 (1986).
3. I. Sobczak, J. S. Lolkema, The 2-hydroxycarboxylate transporter family: Physiology, structure, and mechanism. *Microbiol. Mol. Biol. Rev.* **69**, 665–695 (2005).
4. I. Sobczak, J. S. Lolkema, Loop VIII/IX of the Na+-citrate transporter CitS of *Klebsiella pneumoniae* folds into an amphipathic surface helix. *Biochemistry* **44**, 5461–5470 (2005).
5. I. Sobczak, J. S. Lolkema, Structural and mechanistic diversity of secondary transporters. *Curr. Opin. Microbiol.* **8**, 161–167 (2005).
6. J. S. Lolkema, D. J. Slotboom, Structure and elevator mechanism of the Na^+-citrate transporter CitS. *Curr. Opin. Struct. Biol.* **45**, 1–9 (2017).
7. Y. Huang, M. J. Lemieux, J. Song, M. Auer, D. N. Wang, Structure and mechanism of the glycerol-3-phosphate transporter from *Escherichia coli*. *Science* **301**, 616–620 (2003).
8. J. Abramson *et al.*, Structure and mechanism of the lactose permease of *Escherichia coli*. *Science* **301**, 610–615 (2003).
9. N. Reyes, C. Ginter, O. Boudker, Transport mechanism of a bacterial homologue of glutamate transporters. *Nature* **462**, 880–885 (2009).
10. V. Arkhipova, A. Guskov, D. J. Slotboom, Structural ensemble of a glutamate transporter homologue in lipid nanodisc environment. *Nat. Commun.* **11**, 998 (2020).
11. D. Wöhlert, M. J. Grötzinger, W. Kühlbrandt, Ö. Yildiz, Mechanism of Na(+)-dependent citrate transport from the structure of an asymmetrical CitS dimer. *eLife* **4**, e09375 (2015).
12. T. Uchihashi *et al.*, Dynamic structural states of ClpB involved in its disaggregation function. *Nat. Commun.* **9**, 2147 (2018).
13. S. Maity *et al.*, VPS4 triggers constriction and cleavage of ESCRT-III helical filaments. *Sci. Adv.* **5**, eaau7198 (2019).
14. A. Valbuena, S. Maity, M. G. Mateu, W. H. Roos, Visualization of single molecules building a viral capsid protein lattice through stochastic pathways. *ACS Nano* **14**, 8724–8734 (2020).
15. K. X. Ngo, N. Kodera, E. Katayama, T. Ando, T. Q. Uyeda, Cofilin-induced unidirectional cooperative conformational changes in actin filaments revealed by high-speed atomic force microscopy. *eLife* **4**, e04806 (2015).
16. Y. Ruan *et al.*, Direct visualization of glutamate transporter elevator mechanism by high-speed AFM. *Proc. Natl. Acad. Sci. U.S.A.* **114**, 1584–1588 (2017).
17. T. Haruyama *et al.*, Single-unit imaging of membrane protein-embedded nanodiscs from two oriented sides by high-speed atomic force microscopy. *Structure* **27**, 152–160.e3 (2019).
18. C. N. Kästner, P. Dimroth, K. M. Pos, The Na+-dependent citrate carrier of *Klebsiella pneumoniae*: High-level expression and site-directed mutagenesis of asparagine-185 and glutamate-194. *Arch. Microbiol.* **174**, 67–73 (2000).
19. J. S. Lolkema, H. Enequist, M. E. van der Rest, Transport of citrate catalyzed by the sodium-dependent citrate carrier of *Klebsiella pneumoniae* is obligatorily coupled to the transport of two sodium ions. *Eur. J. Biochem.* **220**, 469–475 (1994).
20. J. S. Lolkema, D. J. Slotboom, Models to determine the kinetic mechanisms of ion-coupled transporters. *J. Gen. Physiol.* **151**, 369–380 (2019).
21. J. S. Lolkema, D. J. Slotboom, The Hill analysis and co-ion-driven transporter kinetics. *J. Gen. Physiol.* **145**, 565–574 (2015).
22. G. Trinco *et al.*, Kinetic mechanism of Na^+-coupled aspartate transport catalyzed by Glt_{Tk}. *Commun. Biol.* **4**, 751 (2021).
23. J. W. Kim *et al.*, Structural insights into the elevator-like mechanism of the sodium/citrate symporter CitS. *Sci. Rep.* **7**, 2548 (2017).
24. F. Kebbel, M. Kurz, M. Arheit, M. G. Grütter, H. Stahlberg, Structure and substrate-induced conformational changes of the secondary citrate/sodium symporter CitS revealed by electron crystallography. *Structure* **21**, 1243–1250 (2013).

25. I. Sgouralis, S. Pressé, An introduction to infinite HMMs for single-molecule data analysis. *Biophys. J.* **112**, 2021–2029 (2017).
26. G. Verdon, O. Boudker, Crystal structure of an asymmetric trimer of a bacterial glutamate transporter homolog. *Nat. Struct. Mol. Biol.* **19**, 355–357 (2012).
27. G. Verdon, S. Oh, R. N. Serio, O. Boudker, Coupled ion binding and structural transitions along the transport cycle of glutamate transporters. *eLife* **3**, e02283 (2014).
28. T. R. Matin, G. R. Heath, G. H. M. Huysmans, O. Boudker, S. Scheuring, Millisecond dynamics of an unlabeled amino acid transporter. *Nat. Commun.* **11**, 5016 (2020).
29. G. B. Erkens, I. Hänelt, J. M. Goudsmits, D. J. Slotboom, A. M. van Oijen, Unsynchronised subunit motion in single trimeric sodium-coupled aspartate transporters. *Nature* **502**, 119–123 (2013).
30. G. Sudha *et al.*, The evolutionary history of topological variations in the CPA/AT transporters. *PLOS Comput. Biol.* **17**, e1009278 (2021).
31. K. I. Okazaki *et al.*, Mechanism of the electroneutral sodium/proton antiporter PaNhaP from transition-path shooting. *Nat. Commun.* **10**, 1742 (2019).
32. A. A. Garaeva, D. J. Slotboom, Elevator-type mechanisms of membrane transport. *Biochem. Soc. Trans.* **48**, 1227–1241 (2020).
33. I. Hänelt, S. Jensen, D. Wunnicke, D. J. Slotboom, Low affinity and slow Na+ binding precedes high affinity aspartate binding in the secondary-active transporter GltPh. *J. Biol. Chem.* **290**, 15962–15972 (2015).
34. J. Knol, K. Sjollema, B. Poolman, Detergent-mediated reconstitution of membrane proteins. *Biochemistry* **37**, 16410–16415 (1998).
35. N. Kodera *et al.*, Structural and dynamics analysis of intrinsically disordered proteins by high-speed atomic force microscopy. *Nat. Nanotechnol.* **16**, 181–189 (2021).
36. S. Maity *et al.*, Caught in the act: Mechanistic insight into supramolecular polymerization-driven self-replication from real-time visualization. *J. Am. Chem. Soc.* **142**, 13709–13717 (2020).
37. T. Uchihashi, N. Kodera, T. Ando, Guide to video recording of structure dynamics and dynamic processes of proteins by high-speed atomic force microscopy. *Nat. Protoc.* **7**, 1193–1206 (2012).
38. N. Kodera, H. Abe, P. D. N. Nguyen, S. Ono, Native cyclase-associated protein and actin from *Xenopus laevis* oocytes form a unique 4:4 complex with a tripartite structure. *J. Biol. Chem.* **296**, 100649 (2021).
39. C. D. Kinz-Thompson, N. A. Bailey, R. L. Gonzalez Jr., Precisely and accurately inferring single-molecule rate constants. *Methods Enzymol.* **581**, 187–225 (2016).